Published in final edited form as:
Nature. ; 478(7369): 408–411. doi:10.1038/nature10450.

Crystal structure of a bacterial homologue of the bile acid sodium symporter ASBT

Nien-Jen Hu[1,2,3], **So Iwata**[1,2,3,4,5,*], **Alexander D. Cameron**[1,2,3,4,*], and **David Drew**[1,*]

[1]Division of Molecular Biosciences, Imperial College London, London, SW7 2AZ, U.K.

[2]Membrane Protein Laboratory, Diamond Light Source, Harwell Science and Innovation Campus, Didcot, Chilton, Oxfordshire, OX11 0DE, U.K.

[3]Research Complex at Harwell Rutherford, Appleton Laboratory, Harwell, Oxford, Didcot, Oxfordshire, OX11 0FA, U.K.

[4]Japan Science and Technology Agency, ERATO, Human Crystallography Project, Yoshida Konoe, Sakyo-ku, Kyoto 606-851, Japan.

[5]Department of Cell Biology, Graduate School of Medicine, Kyoto University, Yoshida-Konoe, Sakyo-ku, Kyoto 606-8501, Japan.

Abstract

High cholesterol levels greatly increase the risk of cardiovascular disease. By its conversion into bile acids, about 50% of cholesterol is eliminated from the body. However bile acids released from the bile duct are constantly recycled, being reabsorbed in the intestine *via* the Apical Sodium dependent Bile acid Transporter (ASBT). It has been shown in animal models that plasma cholesterol levels are significantly lowered by specific inhibitors of ASBT[1,2], thus ASBT is a target for hypercholesterolemia drugs. Here, we describe the crystal structure of a bacterial homologue of ASBT from *Neisseria meningitidis* ($ASBT_{NM}$) at 2.2Å. $ASBT_{NM}$ contains two inverted structural repeats of five transmembrane helices. A Core domain of six helices harbours two sodium ions while the remaining helices form a Panel-like domain. Overall the architecture of the protein is remarkably similar to the sodium-proton antiporter NhaA[3] despite no detectable sequence homology. A bile acid molecule is situated between the Core and Panel domains in a large hydrophobic cavity. Residues near to this cavity have been shown to affect the binding of specific inhibitors of human ASBT[4]. The position of the bile acid together with the molecular architecture suggests the rudiments of a possible transport mechanism.

ASBT/IBAT is a SLC10 (Sodium bile acid co-transporter family) member that moves bile acids across the apical membrane of the ileum into the portal blood vein[5,6]. ASBT utilizes the sodium ion gradient to drive the uphill transport of bile acids across membranes, with a

*Correspondence and request for materials should be addressed to D.D. (d.drew@imperial.ac.uk), A.C. (a.cameron@imperial.ac.uk) or S.I. (s.iwata@imperial.ac.uk). .

Supplementary Information SI Tables 1 and 2 SI Figures 1 to 10

Author contributions N-J.H, S.I, A.C and D.D contributed to the design of the project. N-J.H and D.D. screened homologues, expressed and purified the protein and carried out functional characterization. N-J.H, S.I, A.C and D.D were involved in crystallographic experiments and analysis of data. A.C. and D.D were responsible for overall project management and wrote the manuscript together with assistance from N-J.H and S.I.
The coordinates and the structure factors for $ASBT_{NM}$ and $ASBT_{NM\_1}$ have been deposited in the Protein Data Bank with entries 3ZUY and 3ZUX respectively.

The authors declare no competing financial interests.

Europe PMC Funders Author Manuscripts

stoichiometry of two sodium ions per substrate reported[7]. Mutations in the human ASBT gene cause a condition of primary bile acid malabsorption[8]. ASBT is a pharmaceutical target for drugs aimed at lowering cholesterol and several ASBT inhibitors have been developed that are effective in animal models[1,2]. As some drugs are poorly absorbed in the intestine or need to be targeted to the liver, ASBT and its close liver paralogue NTCP have also received attention as pro-drug carriers, capable of transporting various compounds coupled to bile acid, *e.g*. HMG-CoA reductase inhibitors, the anti-viral drug acyclovir, nucleotides and cytostatic drugs[9].

$ASBT_{NM}$ from *Neisseria meningitidis,* with 26% identity and 54% similarity to human ASBT was identified by fluorescent-based screening methods[10,11] as a suitable candidate for structural studies (Supplementary Fig. 1 and Fig. 2). Residues known to be functionally important in mammalian ASBT and other SLC10 members[12] are well conserved in $ASBT_{NM}$ (Supplementary Fig. 1). Bile acid transport by $ASBT_{NM}$ was confirmed in whole-cells by the sodium-dependent uptake of [^{3}H]-taurocholate (Fig. 1a). The observed K_m for [^{3}H]-taurocholate is in the low μM range ~50μM (Fig. 1b), which is similar to that measured for rat and human ASBT[7,13,14]. The ASBT inhibitors cyclosporin A[15], bromosulfophthalein[15] and the drug Fluvastatin[16], are also competitors for $ASBT_{NM}$-mediated [^{3}H]-taurocholate transport (Fig. 1c). Thus, $ASBT_{NM}$ is a valid model of mammalian bile acid transporters. The $ASBT_{NM}$ structure was solved by single wavelength anomalous scattering and refined at a resolution of 2.2Å (Supplementary Tables 1 and 2, see Methods).

$ASBT_{NM}$ has cytoplasmic N- and C- termini, is comprised of 10 transmembrane helices (TMs) that are linked by short loops, and has overall dimensions of approximately 45 × 30 × 30Å (Figs. 2a and b and Supplementary Fig. 3). TMs 1 to 5 and TMs 6 to 10 are topologically similar but oppositely orientated in the plane of the membrane. The r.m.s.d. (root mean square deviation) after superposition of the two topology-inverted repeats is 3.7Å (Supplementary Fig. 4a and b, and see Methods). Each repeating unit is made of an N-terminal V-motif (TMs 1-2, 6-7) and a Core motif of 3 helices (TMs 3-5, 8-10) (Fig. 2, Supplementary Fig. 3 and 4). If the V and Core-motifs are superposed separately, the r.m.s.d. is lower, 2.6Å and 2.8Å respectively (Supplementary Fig. 4c). The Core motifs from each repeat form the “Core” domain, whereas the two V-motifs create a “Panel” like domain (Fig. 2b). TMs 4 and 9 in the Core domain are broken in the middle (discontinuous), and form helical hairpins with kinked TMs 5 and 10, respectively. At the point where TMs 4 and 9 are broken by well-conserved peptide motifs, they cross over (Fig. 2, Supplementary Fig. 5 and 6)**.** On the intracellular side a wide crevice separates the Core from the Panel domain (Fig. 3a). The cavity extends over halfway through the protein. The extracellular side of the cavity is tightly closed by TMs 1, 2, 4b, 7, 9b and 10. Previously, two topology models of ASBT were proposed with 7 or 9 TMs respectively[17,18]. As TM1 is not conserved in ASBT the structure is broadly consistent with the 9-TM model (Supplementary Fig. 5). TMs 4 and 9 were annotated as extracellular loops in the 7-TM topology model, but were correctly identified in the 9-TM model.

Discontinuous TMs are a common motif in secondary active transporters[3,19,20]. However, the sodium-proton antiporter NhaA is the only other known example where these helices cross as observed in $ASBT_{NM}$ (Supplementary Fig. 6). Indeed, $ASBT_{NM}$ has a similar structure to NhaA, and they superpose with an r.m.s.d. of 2.9Å over 202 C_α atoms (Supplementary Fig. 7a, see Methods). The similarity is more striking when the Core and Panel domains are superposed separately (Supplementary Fig. 7b). This unexpected finding further emphasizes the remarkable plasticity of transporters to utilize a common scaffold to translocate different substrates[20].

In ASBT and NTCP two sodium ions are translocated per bile acid molecule[7,21]. In the highly conserved Core domain of $ASBT_{NM}$ (Supplementary Fig. 8), we have identified two sodium-binding sites (Na1 and Na2) based on the coordination and bond distances (2.0-2.5Å) (Fig. 3b, Supplementary Fig. 9a and 10a, see Methods). Na1, is located approximately 10Å from the cytoplasmic surface between TMs 4b and 5, but also interacts with the carboxylate moiety of Glu260 on TM9a, (Fig. 3b and Supplementary Fig. 10a)**.** The Na2 site is located 8Å from Na1, near the centre at the crossover points of TMs 4a-4b and 9a-9b. Four backbone carbonyl-oxygen atoms coordinate Na2, including Glu260 on TM9a, and the side chains of Gln264 on TM9a and Gln77 on TM3. The residues for which the side-chains interact with the two sodium ions are completely conserved in ASBT and NTCP (Supplementary Figs. 5 and 8). The equivalent glutamate residue to Glu260 is essential for activity in ASBT and NTCP[13,22]. In $ASBT_{NM}$ its replacement with alanine significantly affects transport, as does the mutation of Gln77 to alanine (Fig. 1d and Supplementary Fig. 2a). Thus, it appears that both sodium ions are required for efficient transport. Mechanistically sodium at the Na2 site is almost certainly important to neutralize the partial negative dipole of TM9a, and by doing so, stabilize the interaction with TM4a. Neutralization of the helix dipoles seems a conserved feature for this fold. In NhaA the corresponding TM is thought to be neutralized by the positive charge of Lys300, which is essential for transport[3,23].

The substrate-binding cavity is open to the cytoplasm and is approximately 6 × 12 × 14Å with a solvent accessible volume of $550Å^3$ (Fig. 3a and see Methods). As the N-terminal half of TM1 is profoundly bent outwards it is more open to one side. The cavity is much bigger than taurocholate, perhaps reflecting the large variety of compounds that are recognized by ASBT[9,12,16] (Fig. 3a and c). It is predominantly hydrophobic but near the bottom there are a number of polar residues and water molecules (Fig. 3c and Supplementary Fig. 10b). As judged from high B-factors, taurocholate appears weakly bound (Supplementary Table 2 and Supplementary Fig. 9b). Consistent with this observation there is only one direct hydrogen bond between $ASBT_{NM}$ and taurocholate, from Asn295 on TM10 to the 7α hydroxyl group. The mutation of Asn295 to alanine causes a dramatic reduction in taurocholate transport (Fig. 1d and Supplementary Fig. 2a). Water molecules bridge the 7α hydroxyl with His294 and the 3α hydroxyl with Asn265, located at the crossover region of TM9. Thr112 is also in the vicinity of the 3α group but cannot be unambiguously placed. The 12α hydroxyl group does not have any apparent hydrogen-bonding partner. The taurine moiety binds between TM1 and TM10. Interaction of the taurocholate with residues in TM10 is in agreement with biochemical data, which have proposed that the last helix in ASBT plays a dominant role in the translocation process[24]. The location of Asn265 between the TM4b and 9b dipoles suggests that it may play a role in the mechanism. The importance of this residue has been inferred from mutagenesis studies on NTCP[22]. In $ASBT_{NM}$, if it is replaced by alanine, transporter activity is reduced by ~80% (Fig. 1d and Supplementary Fig 2a). Though there are clear similarities in the binding sites between $ASBT_{NM}$ and ASBT there are also sequence differences (Supplementary Fig. 5). Such differences may affect substrate specificity.

For transport to take place the protein must switch between outward and inward facing states[25]. The architecture of $ASBT_{NM}$ provides a clue to understanding how this might occur. The sodium ions are located in the Core domain close to the crossover points of the discontinuous helices and occluded from the bulk solvent. In NhaA sodium binding causes a rearrangement of these helices[26,27]. In $ASBT_{NM}$ similar rearrangements in the Core domain are therefore likely. Since NhaA only translocates ions[26] these TM movements might be sufficient for transport. However, because $ASBT_{NM}$ transports much larger substrates, structural movements in more than the Core domain are needed. For the sodium-coupled transporter LeuT, Forrest *et al* used the internal asymmetry of the repeating motifs to predict global movements from a single structure[28]; which have been substantiated by crystallographic studies[29]. In an analogous manner to LeuT, an outward-facing model of $ASBT_{NM}$ was generated by superimposing TMs 1-5 on TMs 6-10 and *vice versa* (Fig. 4a and see Methods). Comparing the inward-facing $ASBT_{NM}$ structure with the outward-facing model, the largest difference is the position of the Panel relative to the Core domain (Fig 4c). A route through the protein between these domains is in agreement with experimental data, that suggest that the last helix of ASBT and TM9 of NhaA line the transport pathway[3,24,26,30]. Interestingly, the NhaA domain equivalent to the Panel is placed between that of the outward-facing and inward-facing $ASBT_{NM}$ states (Fig. 4b). This may either be because NhaA translocates a much smaller substrate, or it could represent another conformation of the transporter, likely an occluded state.

In summary, we propose that sodium binding controls the conformation of the Core domain of $ASBT_{NM,}$ which, in turn, drives the movement of the Panel domain. This large conformational change of the Panel relative to the Core domain is required to alter the accessibility to the substrate-binding pocket. The $ASBT_{NM}$ structure should provide important new avenues for designing inhibitors against ASBT with the goal to treat hypercholesterolemia.

Methods Summary

$ASBT_{NM}$ was cloned into a cleavable GFP-His_8 fusion vector pWaldoGFPe[10]. The fusion protein was expressed in *E. coli*, solubilised in 1% dodecyl-β-D-maltopyranoside (DDM) and purified to homogeneity. Prior to crystallisation, untagged $ASBT_{NM}$ was exchanged into 0.06% n-dodecyl-N,N-dimthylamine-N-oxide (LDAO) by size-exclusion chromatography. Crystals were grown in the presence of 10 mM taurocholate by the vapour diffusion method. Data were collected on beamlines I02 and I03 at the Diamond Light Source, dehydration of the crystals being necessary to collect high-resolution data. The protein was derivatised by short soaking a surface engineered cysteine mutant ($ASBT_{NM\_1}$) with 1 mM mercury acetate. The structure of $ASBT_{NM\_1}$ was solved by Hg-SAD and subsequently refined against data collected from $ASBT_{NM}$ at a resolution of 2.2Å. The cell-based bile acid uptake assay for $ASBT_{NM}$ was modified from that previously described[6]

Supplementary Material

Refer to Web version on PubMed Central for supplementary material.

Acknowledgments

We are grateful to, Chiara Lee and Yusuke Sekiguchi for assistance with cloning and expression screening of $ASBT_{NM}$ mutants, and Dr. Stan van de Graaf (Utrecht University) for kindly donating fluorescently labeled bile acid, which was used in the initial functional characterization of $ASBT_{NM}$. Data were collected at the European Synchrotron Radiation Facility and Diamond Light Source, with excellent assistance from beamline scientists, in particular we would like to thank Dr. Juan Sanchez-Weatherby for help with the HCl. We are also grateful to Dr. Konstantinos Beis and Prof. Gunnar von Heijne for critical reading of the manuscript. This work was funded by the European Union (EMeP grant, LSHG-CT-2004-504601 to S.I), and the Medical Research Council (MRC grant, MRC_G0900990, to A.C and D.D). A part of this work was also supported by a grant from the ERATO IWATA Human Receptor Crystallography Project from the Japan Science and Technology Agency. The authors are grateful for the use of the Membrane Protein Laboratory funded by the Wellcome Trust (grant WT089809) at the Diamond Light Source Limited. D.D. acknowledges the personal support from The Royal Society through the University Research Fellow scheme.

METHODS

ASBT$_{NM}$ sequence

MNILSKISSFIGKTFSLWAALFAAAAFFAPDTFKWAGPYIPWLLGIIMFGMGLT
LKPSDFDILFKHPKVVIIGVIAQFAIMPATAWLLSKLLNLPAEIAVGVILVGCCP
GGTASNVMTYLARGNVALSVAVTSVSTLISPLLTPAIFLMLAGEMLEIQAAG
MLMSIVKMVLLPIVLGLIVHKVLGSKTEKLTDALPLVSVAAIVLIIGAVVGAS
KGKIMESGLLIFAVVVLHNGIGYLLGFFAAKWTGLPYDAQKTLTIEVGMQNS
GLAAALAAAHFAAAPVVAVPGALFSVWHNISGSLLATYWAAKAGKHKKPGSENL
YFQ

ASBT$_{NM-1}$ sequence for structure solution

MVAASMNILSKISSFIGKTFSLWAALFAAAAFFAPDTFKWAGPYIPWLLGIIMF
GMGLTLKPSDFDILFKHPKVVIIGVIAQFAIMPATAWCLSKLLNLPAEIAVGVI
LVGCCPGGTASNVMTYLARGNVALSVAVTSVSTLTSPLLTPAIFLMLAGEML
EIQAAGMLMSIVKMVLLPIVLGLIVHKVLGSKTEKLTDALPLVSVAAIVLIIGA
VVGASKGKIMESGLLIFAVVVLHNGIGYLLGFFAAKWTGLPYDAQKALTIEV
GMQNSGLAAALAAAHFAAAPVVAVPGALFSVWHNISGSLLATYWAAKAGK
HKKPLDRAGSENLYFQ

Expression screening, mutagenesis and protein purification

Bacterial ASBT homologues were cloned as GFP-His$_8$ fusions into the vector pWaldoGFPe[31]. Fusions were overexpressed in *Escherichia coli* C43(DE3) cells[32] by the addition of 0.4mM IPTG at an OD_{600} of 0.4. The temperature was lowered to 25 °C for overnight induction. The monodispersity of expressed fusions were screened in crude dodecyl-β-D-maltopyranoside (DDM), decyl-β-D-maltopyranoside (DM), nonyl-β-D-maltopyranoside (NM), n-dodecyl-N,N-dimthylamine-N-oxide (LDAO) or dodecyl nonaethylene glycol ether ($C_{12}E_9$) solubilised membranes by fluorescence-detection size exclusion chromatography (FSEC)[33] as outlined previously[31]. The ASBT$_{NM}$ homologue from *Neiserria meningitidis* (MC58) was selected for structural studies based on the amount of protein produced, as judged by whole-cell[10] and in-gel fluorescence[31], and the quality of the FSEC trace in different detergents. Site directed mutants of ASBT$_{NM}$ were generated by PCR (Quickchange™, Agilent Technologies). Wild-type ASBT$_{NM}$ and mutants were purified essentially as previously described[34] In brief, membranes were isolated from 10-L *E. coli* cultures and solubilised in 1% DDM for 2 hrs in buffer containing 1 × PBS, 150 mM NaCl and 10 mM imidazole. The suspension was cleared by ultracentrifugation at 120, 000 × g for 1 h. The sample was mixed with 1 ml of Ni-NTA Superflow resin (QIAGEN) per 1 mg of GFP-His$_8$ and incubated for 2 hrs at 4°C. Slurry was loaded onto a glass Econo-Column (Bio-Rad) and washed in 1 × PBS buffer containing 0.1% DDM, 150 mM NaCl and 20 mM imidazole for 20 column volumes (CV). Bound material was washed for a further 20 CVs in the same buffer containing 50 mM imidazole. The ASBT$_{NM}$-GFP-His$_8$ fusion was eluted in 2 CVs of the same buffer containing 250 mM imidazole. The eluted protein was dialyzed overnight in the presence of stoichiometric amounts of His$_6$ tagged Tobacco Etch Virus (TEV) protease in 3L of buffer containing 20 mM Tris-HCl, pH 7.5, 150 mM NaCl and 0.03% DDM. Dialyzed sample was passed through a 5-ml Ni-NTA His™-Trap column (GE Healthcare) and the flow through containing ASBT$_{NM}$ collected. Protein was concentrated using 100K MWCO cut-off concentrators to 10 mg/ml and loaded onto a Superdex 200 10/300 gel filtration column (GE Healthcare) equilibrated in 20 mM Tris-HCl, pH 7.5, 0.15 M NaCl and 0.06% LDAO. The choice of the detergent LDAO was considered suitable for crystallization by comparing FSEC[33] and stability data[35] for ASBT$_{NM}$ to membrane proteins known to crystallize in this detergent[11]. The protein peak was collected and concentrated to 20 mg/ml for crystallization.

Transport time course

E. coli cells harboring wild-type $ASBT_{NM}$-GFP-His_8 were harvested and resuspended in uptake buffer consisting of 1 mM $CaCl_2$, 1mM $MgCl_2$, 10 mM Tris-HCl pH 7.5 and 137 mM NaCl (Na^+-containing buffer) or 137 mM choline chloride (Na^+-low buffer). Cells were incubated at 37°C with uptake buffer containing 4 μM taurocholate supplemented with 0.16 μM [2,4-^{3}H]-taurocholate (30 Ci/mmol, American Radiolabelled Chemicals) for indicated time intervals. Transport was terminated by the addition of ice-cold buffer containing 1 mM $CaCl_2$, 1 mM $MgCl_2$, 10 mM Tris-HCl pH 7.5, 137 mM NaCl, 1 mM taurocholate and immediately followed by centrifugation at 20,500 × *g* for 60s. Cell pellets were washed several times in an equal volume of termination buffer, and resuspended in 200 μl of the same buffer. The radioactivity corresponding to the internalized substrate was measured by scintillation counting. Each experiment was performed in triplicate. Non-specific uptake was assessed by repeating the time-course in triplicate for cells transformed with the same vector but expressing the sodium-proton antiporter NhaA-GFP-His_8 fusion. In all experiments, $ASBT_{NM}$ expression was calculated based on GFP fluorescence measured at 510 nm (exc. 488 nm) using a 96-well spectrofluorometer[31]. In-gel fluorescence[31]and FSEC[33] data of DDM solubilised whole-cells of wild-type $ASBT_{NM}$ and mutants were carried out as described previously.

Transport kinetics

The accumulation of taurocholate was linear within the first 120s. For kinetic characterization, the initial velocity of taurocholate uptake at 37°C was measured after 120s at the indicated increasing substrate concentrations. The radioactivity corresponding to the internalized substrate was measured by scintillation counting. Each experiment was performed in triplicate. The data was fitted to the Michaelis-Menten equation by nonlinear regression using the GraphPad Prism™ software.

Activity of $ASBT_{NM}$ Mutants

E. coli cells harboring $ASBT_{NM}$-GFP-His_8 mutants were resuspended in uptake buffer containing 4 μM taurocholate supplemented with 0.16 μM of [2,4-^{3}H]-taurocholate (30 Ci/mmol, American Radiolabelled Chemicals) for 5 mins at 37°C. The radioactivity corresponding to the internalized substrate was measured by scintillation counting. For each mutant the uptake values were corrected for background by subtracting those from parallel assays carried out in the absence of sodium. Activities were plotted as percentage of the wild type transport activity calculated in the same way. Each experiment was performed in triplicate.

Substrate specificity

The whole-cell [^{3}H]-taurocholate uptake assay was carried out similarly to that described for $ASBT_{NM}$ mutants, except that 150 μM of either taurocholate (Sigma), cyclosporin A (Sigma), bromosulfophthalein (Sigma) or fluvastatin (Cayman Europe) was added to the uptake buffer.

Crystallisation and preliminary screening

Crystals were grown at 20°C using the vapour diffusion method. Taurocholic acid (Sigma) was added to the protein solution to a final concentration of 10 mM. The protein was then mixed 1:1 with reservoir solution containing 50 mM sodium citrate pH 4.5, 70 mM NaCl, and 22-24% PEG 400. Crystals appeared overnight and reached a maximum size after 3-4

Europe PMC Funders Author Manuscripts

days. The crystals were frozen in liquid nitrogen and screened using synchrotron radiation at the European Synchrotron Radiation Facility (Grenoble, France) and Diamond Light Source (Harwell, U.K.). Crystals are tetragonal with cell dimensions of approximately 75 × 75 × 180Å. The best of these crystals diffract to around 2.8 to 3.5Å, however with dehydration the diffraction is increased to ~2Å.

Structure Determination of a Cysteine Mutant of $ASBT_{NM}$

As initial attempts at making heavy atom derivatives with mercury compounds failed, Leu 87 was modified to cysteine (construct $ASBT_{NM-1}$). The $ASBT_{NM-1}$ protein crystallized similarly to the wild-type protein. Mercury derivitized crystals were obtained from this mutant by incubating for 1 hr with 1 mM mercury acetate prior to crystallization. A single mercury derivatised crystal of $ASBT_{NM\_1}$ was used to solve the structure by SAD. The crystal was frozen in liquid nitrogen and then reannealed before data collection by leaving in air for approximately 3 mins. The reannealing resulted in shrinkage of the unit cell and an increase in the resolution to 2.2Å. Data were collected at the Hg edge (1.0060Å) on beamline I03 at the Diamond Light Source. Data were initially processed to 2.5Å by the Xia2[36] pipeline to XDS[37] set up on the beamline with further processing using the CCP4 suite of programs[38]. The space group was determined to be $P4_122$ with one molecule in the asymmetric unit. An anomalous difference Patterson map showed clear peaks associated with one bound heavy atom. The heavy atom coordinates were determined using RSPS[39]. Its position was refined and phases were calculated using SHARP[40] with solvent flattening in Solomon[41]. The resulting phases were input to the automatic structure building implemented in Phenix[42]. This resulted in a model that was reasonably complete. Modification and further building of the structure was carried out in O[43] and Coot[44]. At this point the data were reprocessed using Mosflm[45], extending the resolution to 2.2Å as judged from the scaling statistics (Supplementary Table 1) and the features in the resulting maps. Structural refinement was performed in BUSTER[46] using individual isotropic B-factor refinement and TLS[47]. The complete protein was chosen as a single TLS group as no significant drop in the R-free was observed when splitting the protein into multiple groups. Two ions were identified in the core of the protein. The residues coordinating these ions and the associated distances are consistent with sodium[48]. As an additional verification the sodium ions were changed to water molecules and run through the program WASP[49], which uses valence calculations to identify possible metal ions. Indeed, only the sodium ions changed to waters were flagged as likely sodium ions. After all residues had been modeled, clear electron density remained in the cavity of the protein. This density was enhanced in a simulated annealing omit map calculated in Phenix[42]. Taurocholate, downloaded from the Cambridge Structural Database (accession code KORZUM), clearly fitted the density with the cholate headgroup positioned into the bottom of the cavity (Supplementary Fig. 9b). A further taurocholate was observed in the crystal interface. The final model has an R-factor 19.7% and a corresponding R-free of 22.9% and contains all protein residues from 2 to 309, 2 sodium ions, 1 Hg, 2 taurocholate molecules, 37 water molecules, 5 LDAO molecules and 2 truncated phospholipids (phosphatidylethanolamine). The final refinement statistics of this model, which was used to solve the wild type protein, are summarized in Supplementary Table 2.

Structure Determination and Refinement of $ASBT_{NM}$

As the reannealing of the $ASBT_{NM-1}$ in air was not reproducible, dehydration was attempted on the humidity controller HC1 device[50] mounted on beamline I02 at Diamond Light Source. By placing the crystal into an air-stream at 45% relative humidity for 5 minutes prior to freezing, crystals were found to reproducibly diffract to ~2.0Å. Data were collected from a single crystal of $ASBT_{NM}$ on I02 at Diamond Light Source. The data were processed in XDS[37] using the Xia2 pipeline[36] and scaled at a resolution of 2.2Å (see Supplementary

Table). The structure was refined, as above, starting from the final model of the $ASBT_{NM-1}$ construct, less all non-protein residues. No appreciable differences were observed in the wild type and mercury derivatised structures. As for $ASBT_{NM-1}$ the resulting electron maps for $ASBT_{NM}$ showed the same position of taurocholate and detergent molecules. The final model has an R-factor of 21.2% and an R-free of 24.4% (Supplementary Table 2).

Structural Analysis

Superpositions were carried out in Lsqman[51]. The superpositions were performed so that only C_α pairs which were less than 3.8Å apart were included in the calculation. The numbers quoted in the text regarding the topology-inverted repeats of $ASBT_{NM}$ are calculated between pairs of C_α atoms that are less than 10Å apart. This was considered necessary so as to include atoms from both the V and Core motifs. In comparing $ASBT_{NM}$ with NhaA (1ZCD) only pairs of atoms less than 5Å after superposition were chosen giving an r.m.s.d. of 2.9Å for 202 out of a possible 308 pairs of C_a atoms. The volume of the cavity was calculated in Voidoo[52] using a probe radius of 1.4Å. Figures showing the structure were drawn using Pymol[53] except those showing electron density, which were made using the CCP4mg[54].

Outward-facing model

In $ASBT_{NM}$ like LeuT[55], the protein is made up of two 5-TM repeats that when superimposed show a small rotation of two TMs with respect to the other three (Supplementary Fig. 4). For LeuT it was shown that by swapping the conformations of the N and C terminal topology-inverted repeats the structure changes from outward to inward-facing[28]. In $ASBT_{NM}$ the lengths of the two topology-inverted repeats are very similar. To create an outward-facing backbone model of $ASBT_{NM}$, in an analogous manner to that carried out for LeuT, TMs 1-5 were superposed on TMs 6-10 and *vice versa*.

References

1. Lewis MC, Brieaddy LE, Root C. Effects of 2164U90 on ileal bile acid absorption and serum cholesterol in rats and mice. J. Lipid Res. 1995; 36:1098–1105. [PubMed: 7658158]
2. Bhat BG, et al. Inhibition of ileal bile acid transport and reduced atherosclerosis in apoE-/- mice by SC-435. J. Lipid Res. 2003; 44:1614–1621. [PubMed: 12810816]
3. Hunte C, et al. Structure of a Na+/H+ antiporter and insights into mechanism of action and regulation by pH. Nature. 2005; 435:1197–1202. [PubMed: 15988517]
4. Hallen S, Bjorquist A, Ostlund-Lindqvist AM, Sachs G. Identification of a region of the ileal-type sodium/bile acid cotransporter interacting with a competitive bile acid transport inhibitor. Biochemistry. 2002; 41:14916–14924. [PubMed: 12475240]
5. Hagenbuch B, Dawson P. The sodium bile salt cotransport family SLC10. Pflugers Arch. 2004; 447:566–570. [PubMed: 12851823]
6. Wong MH, Oelkers P, Craddock AL, Dawson PA. Expression cloning and characterization of the hamster ileal sodium-dependent bile acid transporter. J. Biol. Chem. 1994; 269:1340–1347. [PubMed: 8288599]
7. Weinman SA, Carruth MW, Dawson PA. Bile acid uptake via the human apical sodium-bile acid cotransporter is electrogenic. J. Biol. Chem. 1998; 273:34691–34695. [PubMed: 9856990]
8. Oelkers P, Kirby LC, Heubi JE, Dawson PA. Primary bile acid malabsorption caused by mutations in the ileal sodium-dependent bile acid transporter gene (SLC10A2). J. Clin. Invest. 1997; 99:1880–1887. [PubMed: 9109432]
9. Kramer W, Wess G. Bile acid transport systems as pharmaceutical targets. Eur. J. Clin. Invest. 1996; 26:715–732. [PubMed: 8889434]
10. Drew D, Lerch M, Kunji E, Slotboom DJ, de Gier JW. Optimization of membrane protein overexpression and purification using GFP fusions. Nat. Methods. 2006; 3:303–313. [PubMed: 16554836]

Europe PMC Funders Author Manuscripts

11. Sonoda Y, et al. Benchmarking membrane protein detergent stability for improving throughput of high-resolution X-ray structures. Structure. 2011; 19:17–25. [PubMed: 21220112]
12. Geyer J, Wilke T, Petzinger E. The solute carrier family SLC10: more than a family of bile acid transporters regarding function and phylogenetic relationships. Naunyn Schmiedebergs Arch. Pharmacol. 2006; 372:413–431. [PubMed: 16541252]
13. Sun AQ, Balasubramaniyan N, Chen H, Shahid M, Suchy FJ. Identification of functionally relevant residues of the rat ileal apical sodium-dependent bile acid cotransporter. J. Biol. Chem. 2006; 281:16410–16418. [PubMed: 16608845]
14. Chignard N, et al. Bile acid transport and regulating functions in the human biliary epithelium. Hepatology. 2001; 33:496–503. [PubMed: 11230727]
15. Craddock AL, et al. Expression and transport properties of the human ileal and renal sodium-dependent bile acid transporter. Am. J. Physiol. 1998; 274:G157–169. [PubMed: 9458785]
16. Zheng X, Ekins S, Raufman JP, Polli JE. Computational models for drug inhibition of the human apical sodium-dependent bile acid transporter. Mol. Pharm. 2009; 6:1591–1603. [PubMed: 19673539]
17. Banerjee A, Swaan PW. Membrane topology of human ASBT (SLC10A2) determined by dual label epitope insertion scanning mutagenesis. New evidence for seven transmembrane domains. Biochemistry. 2006; 45:943–953. [PubMed: 16411770]
18. Hallen S, Branden M, Dawson PA, Sachs G. Membrane insertion scanning of the human ileal sodium/bile acid co-transporter. Biochemistry. 1999; 38:11379–11388. [PubMed: 10471288]
19. Screpanti E, Hunte C. Discontinuous membrane helices in transport proteins and their correlation with function. J. Struct. Biol. 2007; 159:261–267. [PubMed: 17350860]
20. Boudker O, Verdon G. Structural perspectives on secondary active transporters. Trends Pharmacol. Sci. 2010; 31:418–426. [PubMed: 20655602]
21. Hagenbuch B, Meier PJ. Sinusoidal (basolateral) bile salt uptake systems of hepatocytes. Semin. Liver Dis. 1996; 16:129–136. [PubMed: 8781018]
22. Zahner D, Eckhardt U, Petzinger E. Transport of taurocholate by mutants of negatively charged amino acids, cysteines, and threonines of the rat liver sodium-dependent taurocholate cotransporting polypeptide Ntcp. Eur. J. Biochem. 2003; 270:1117–1127. [PubMed: 12631271]
23. Olkhova E, Hunte C, Screpanti E, Padan E, Michel H. Multiconformation continuum electrostatics analysis of the NhaA Na+/H+ antiporter of Escherichia coli with functional implications. Proc. Natl. Acad. Sci. U S A. 2006; 103:2629–2634. [PubMed: 16477015]
24. Hussainzada N, Banerjee A, Swaan PW. Transmembrane domain VII of the human apical sodium-dependent bile acid transporter ASBT (SLC10A2) lines the substrate translocation pathway. Mol. Pharmacol. 2006; 70:1565–1574. [PubMed: 16899538]
25. Jardetzky O. Simple allosteric model for membrane pumps. Nature. 1966; 211:969–970. [PubMed: 5968307]
26. Padan E. The enlightening encounter between structure and function in the NhaA Na+-H+ antiporter. Trends Biochem. Sci. 2008; 33:435–443. [PubMed: 18707888]
27. Appel M, Hizlan D, Vinothkumar KR, Ziegler C, Kuhlbrandt W. Conformations of NhaA, the Na +/H+ exchanger from Escherichia coli, in the pH-activated and ion-translocating states. J. Mol. Biol. 2009; 388:659–672. [PubMed: 19396973]
28. Forrest LR, et al. Mechanism for alternating access in neurotransmitter transporters. Proc. Natl. Acad. Sci. U S A. 2008; 105:10338–10343. [PubMed: 18647834]
29. Shimamura T, et al. Molecular basis of alternating access membrane transport by the sodium-hydantoin transporter Mhp1. Science. 2010; 328:470–473. [PubMed: 20413494]
30. Tzubery T, Rimon A, Padan E. Structure-based functional study reveals multiple roles of transmembrane segment IX and loop VIII-IX in NhaA Na+/H+ antiporter of Escherichia coli at physiological pH. J. Biol. Chem. 2008; 283:15975–15987. [PubMed: 18387952]

References

31. Drew DE, von Heijne G, Nordlund P, de Gier JW. Green fluorescent protein as an indicator to monitor membrane protein overexpression in Escherichia coli. FEBS Lett. 2001; 507:220–224. [PubMed: 11684102]

32. Miroux B, Walker JE. Over-production of proteins in Escherichia coli: mutant hosts that allow synthesis of some membrane proteins and globular proteins at high levels. J. Mol. Biol. 1996; 260:289–298. [PubMed: 8757792]

33. Kawate T, Gouaux E. Fluorescence-detection size-exclusion chromatography for precrystallization screening of integral membrane proteins. Structure. 2006; 14:673–681. [PubMed: 16615909]

34. Drew D, et al. GFP-based optimization scheme for the overexpression and purification of eukaryotic membrane proteins in Saccharomyces cerevisiae. Nat. Protoc. 2008; 3:784–798. [PubMed: 18451787]

35. Alexandrov AI, Mileni M, Chien EY, Hanson MA, Stevens RC. Microscale fluorescent thermal stability assay for membrane proteins. Structure. 2008; 16:351–359. [PubMed: 18334210]

36. Winter G. Xia2: an expert system for macromolecular crystallography data reduction. Journal of Appl. Crystallogr. 2010; 43:186–190.

37. Kabsch W. XDS. Acta Crystallogr. D. 2010; 66:125–132. [PubMed: 20124692]

38. Collaborative Computational Project Number 4. The CCP4 suite: programs for protein crystallography. Acta Crystallogr. D. 1994; 50:760–763. [PubMed: 15299374]

39. Knight SD. RSPS version 4.0: a semi-interactive vector-search program for solving heavy-atom derivatives. Acta Crystallogr. D. 2000; 56:42–47. [PubMed: 10666625]

40. de La Fortelle E, Bricogne G, Charles W, Carter. Maximum-likelihood heavy-atom parameter refinement for multiple isomorphous replacement and multiwavelength anomalous diffraction methods. Methods in Enzymology. 1997; 276:472–494.

41. Abrahams JP, Leslie AGW. Methods used in the structure determination of bovine mitochondrial F1 ATPase. Acta Crystallogr. D. 1996; 52:30–42. [PubMed: 15299723]

42. Adams PD, et al. PHENIX: a comprehensive Python-based system for macromolecular structure solution. Acta Crystallogr. D. 2010; 66:213–221. [PubMed: 20124702]

43. Jones TA, Kjeldgaard M, Charles WC Jr. Robert MS. Electron-density map interpretation. Methods in Enzymology. 1997; 277:173–208. [PubMed: 18488310]

44. Emsley P, Cowtan K. Coot: model-building tools for molecular graphics. Acta Crystallogr. D. 2004; 60:2126–2132. [PubMed: 15572765]

45. Leslie AGW. Recent changes to the MOSFLM package for processing film and image plate data. Joint CCP4 + ESF-EAMCB Newsletter on Protein Crystallography. 1992; (No. 26)

46. Blanc E, et al. Refinement of severely incomplete structures with maximum likelihood in BUSTER-TNT. Acta Crystallogr. D. 2004; 60:2210–2221. [PubMed: 15572774]

47. Winn MD, Isupov MN, Murshudov GN. Use of TLS parameters to model anisotropic displacements in macromolecular refinement. Acta Crystallogr. D. 2001; 57:122–133. [PubMed: 11134934]

48. Harding MM. Metal-ligand geometry relevant to proteins and in proteins: sodium and potassium. Acta Crystallogr. D. 2002; 58:872–874. [PubMed: 11976508]

49. Nayal M, Di Cera E. Valence screening of water in protein crystals reveals potential Na+ binding sites. J. Mol. Biol. 1996; 256:228–234. [PubMed: 8594192]

50. Sanchez-Weatherby J, et al. Improving diffraction by humidity control: a novel device compatible with X-ray beamlines. Acta Crystallogr. D. 2009; 65:1237–1246. [PubMed: 19966409]

51. Kleywegt GJ, Jones TA. A super position. ESF/CCP4 Newsletter. 1994; 31:9.

52. Kleywegt GJ, Jones TA. Detection, delineation, measurement and display of cavities in macromolecular structures. Acta Crystallogr. D. 1994; 50:178–185. [PubMed: 15299456]

53. Delano, WL. The PyMOL Molecular Graphics System. DeLano Scientific; Palo Alto, CA, USA: 2002.

54. Potterton L, et al. Developments in the CCP4 molecular-graphics project. Acta Crystallogr. D. 2004; 60:2288–2294. [PubMed: 15572783]

55. Yamashita A, Singh SK, Kawate T, Jin Y, Gouaux E. Crystal structure of a bacterial homologue of Na+/Cl−-dependent neurotransmitter transporters. Nature. 2005; 437:215–223. [PubMed: 16041361]

Europe PMC Funders Author Manuscripts

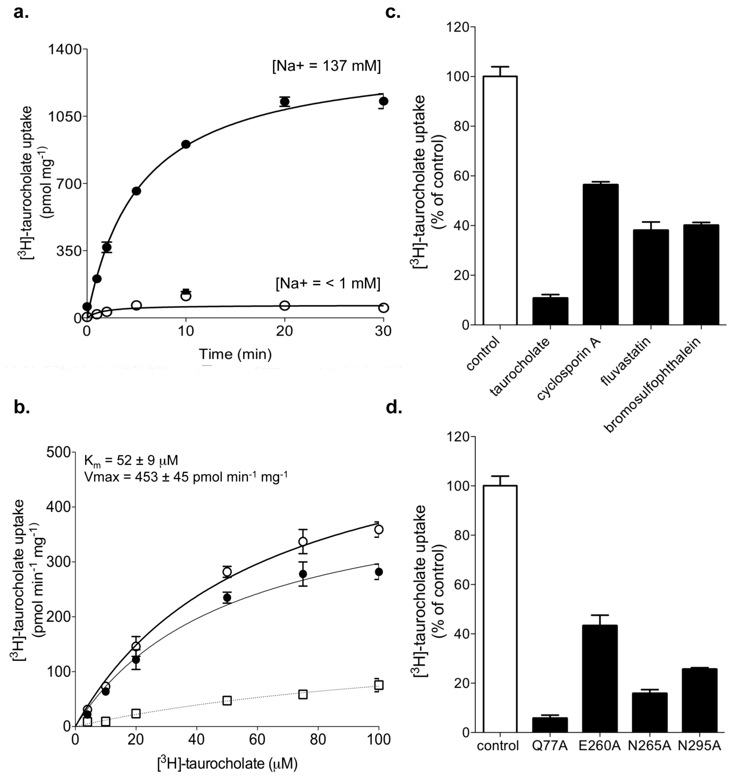

Fig. 1. Sodium-dependent transport of bile acid by $ASBT_{NM}$

a, Time-dependent uptake of $[^3H]$-taurocholate after expression of $ASBT_{NM}$ in *E. coli* as monitored in buffer containing 137 mM sodium (filled circles) or <1 mM sodium (non-filled circles) **b,** Michaelis-Menten transport kinetics of $ASBT_{NM}$-mediated $[^3H]$-taurocholate uptake. The Specific uptake (filled circles) was calculated by subtracting the internalization measured from control cells lacking the transporter (non-filled squares) from the total uptake (non-filled circles), as detailed in Methods. **c,** $ASBT_{NM}$-mediated $[^3H]$-taurocholate uptake after 5 min in the presence of 150 μM of taurocholate, cyclosporin A, fluvastatin or bromosulfophthalein (black-filled bars) measured as a percentage of the uptake without their addition (non-filled bar). **d**, $ASBT_{NM}$-mediated $[^3H]$-taurocholate uptake after 5 min for wild-type (non-filled bar) and single alanine point mutants (filled-bars): Q77A, E260A, N265A and N295A. The uptake for the mutants is displayed as a percentage of the wild type activity. The expression and detergent-solubilised folded-state of all mutants was similar to wild-type protein, Supplementary Fig. 2a. In all experiments errors bars, s.e.m.; n = 3.

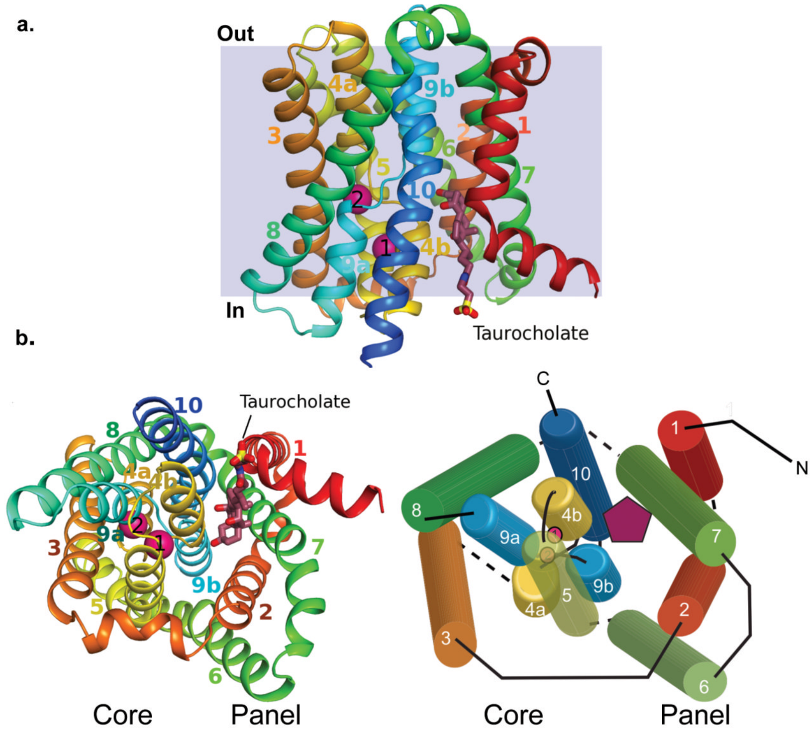

Fig. 2. ASBT$_{NM}$ structure

a, Ribbon representation of ASBT$_{NM}$ as viewed in the plane of the membrane. TMs 1 to 10 have been coloured from red at the N-terminus to blue at the C-terminus and the position of the membrane is depicted in grey. The pink circles indicate sodium sites, Na1/Na2, and the wine-red stick model the substrate taurocholate. **b**, ASBT$_{NM}$ structure as viewed from the intracellular side as a ribbon representation (left) and as a simplified cartoon (right): sodium ions (pink spheres), taurocholate stick model (wine red).

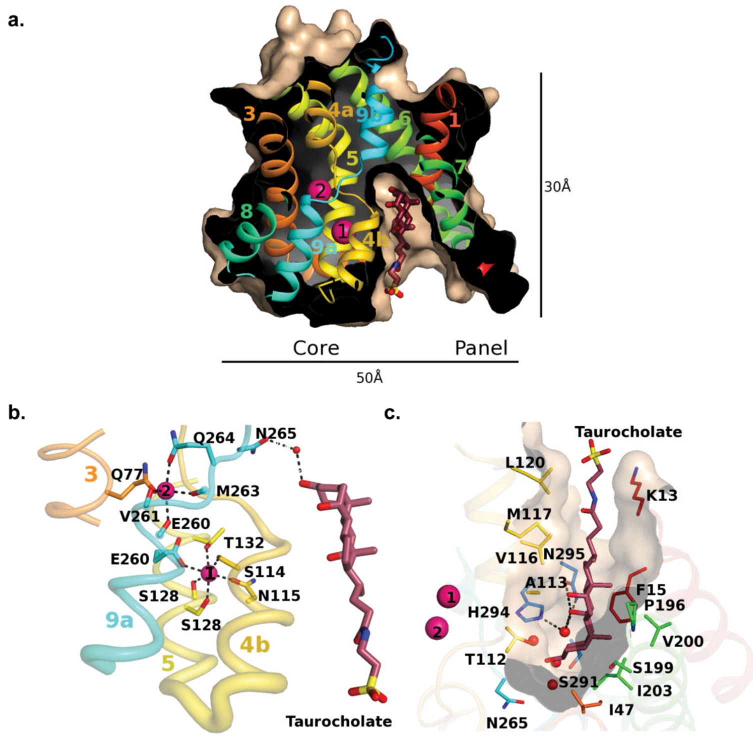

Fig. 3. ASBT$_{NM}$ structure is inward-facing and contains bound sodium and bile acid

a, Surface representation showing the location of the taurocholate-bound intracellular cavity as a section through the protein. **b**, The sodium binding sites in ASBT$_{NM}$. Na1 is octahedrally coordinated by Ser114 and Asn115 on TM4b, Thr132, and Ser128 on TM5 and Glu260 on TM9a. The square pyramidal arrangement of the Na2 ligands is made up of Glu260, Val261, Met263 and Gln264 on TM9, and Gln77 on TM3. **c**, The intracellular cavity in ASBT$_{NM}$. Residues lining the cavity and near to the taurocholate are shown. The figures have been coloured as in Fig. 2. A 150-fold difference in inhibition of the mouse and human forms of ASBT by benzothiazepines[4] has been assigned to sequence differences corresponding to Ser291 at the bottom of the cavity. Supplementary Figure 10 shows a stereo version of b and c.

Europe PMC Funders Author Manuscripts

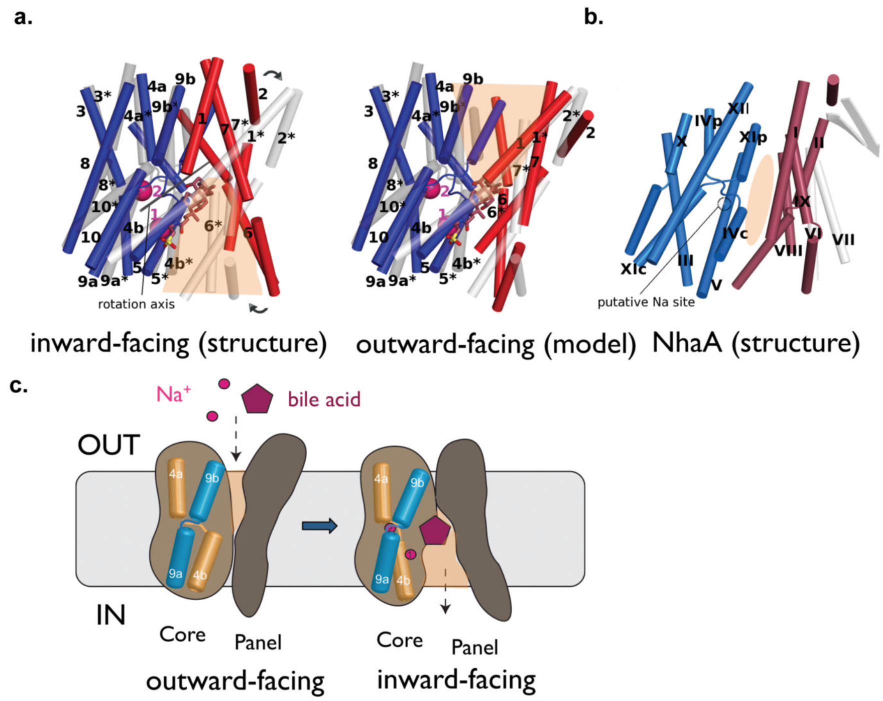

Fig. 4. Putative mechanism for ASBT$_{NM}$ transport

a, Superposition of ASBT$_{NM}$ (red Panel, blue Core) and the outward-facing model as described in the text (light grey). The superposition has been optimized on the Core domains. Loops have been removed for clarity. In the image on the right the Panel of the model has been rotated 25° relative to the Core domain, around the axis shown in the left image, to superimpose the Panels. Significant kinks in the helices are represented as breaks. The area of the cavity is depicted by a salmon trapezoid. **b**, NhaA shown in the same view as ASBT$_{NM}$ in a. The Core domain is shown in light blue and the Panel in brown. The two additional TMs and β-strands that are not present in ASBT$_{NM}$ are shown in grey. The position that sodium is thought to bind[3] is shown with a black ring. **c**, Schematic of the proposed mechanism that illustrates the movement of the Panel against the Core domain to transport sodium and bile acid.